



Confined FeNi alloy nanoparticles in carbon nanotubes for photothermal oxidative dehydrogenation of ethane by carbon dioxide

Jinqiang Zhang^a, Meng Li^b, Xiaojie Tan^b, Lei Shi^c, Kun Xie^d, Xiaoli Zhao^e, Shuaijun Wang^e, Shiyong Zhao^a, Huayang Zhang^a, Xiaoguang Duan^a, Haijun Chen^{d,*}, Yuezhao Zhu^d, Mingbo Wu^b, Hongqi Sun^{e,*}, Shaobin Wang^{a,*}

^a School of Chemical Engineering, The University of Adelaide, North Terrace, Adelaide, SA 5005, Australia

^b State Key Laboratory of Heavy Oil Processing, Institute of New Energy, College of Chemical Engineering, China University of Petroleum (East China), Qingdao 266580, China

^c College of Materials Science and Engineering, Nanjing Forestry University, 210037 Nanjing, China

^d Jiangsu Key laboratory of Process Enhancement and New Energy Equipment Technology, School of Mechanical and Power Engineering, Nanjing Tech University, Nanjing 211816, Jiangsu, China

^e School of Science, Edith Cowan University, 270 Joondalup Drive, Joondalup, WA 6027, Australia

ARTICLE INFO

Keywords:

Non-noble metallic catalyst
Photothermal catalysis
Confinement effect
Light bands contribution
Oxidative dehydrogenation of ethane

ABSTRACT

Oxidative dehydrogenation of ethane with CO₂ (ODEC) is an attractive reaction for reduction of carbon footprints and ethene production. In this work, we present photothermal catalysis on confined bimetal catalysts for ODEC. Carbon nanotubes confined non-noble bimetal alloy (i.e., CoNi@CNTs and FeNi@CNTs) catalysts were prepared and FeNi@CNTs showed effective performance in photothermal catalytic ODEC to ethene. Experiments and simulations reveal that UV and visible lights (420 – 490 nm) are responsible for ODEC and non-oxidative dehydrogenation of ethane, respectively, to ethene. Additionally, ODEC to ethene is preferred to C-C cracking to methane on FeNi@CNTs in light (> 490 nm)-induced thermocatalysis. The photothermal effect turns more significant when introduced into thermocatalytic ODEC (500 °C), with ethene generation at one order of magnitude. This work advances new mechanism of photo-mediated catalysis and sheds light on utilization of full-spectrum solar energy and non-noble metallic catalysts for ethene production and CO₂ recycling at moderate conditions.

1. Introduction

Ethene as one of the most essential chemical feedstocks is widely used for synthesis of fibers, rubbers, plastics, and other value-added chemicals, and its yield is always taken as an index to measure the capacity of petrochemical industry [1]. At present, ethene used in chemical industry is mainly separated from gaseous products of petroleum oils. Due to the shortage of oil resources, ethane as one source to ethene has abundant reserves in natural gas [2]. Therefore, dehydrogenation of ethane is deemed as a promising route for ethene production. However, the strong C-H bond (423 kJ/mol) of ethane enables non-oxidative dehydrogenation of ethane (NODE) process low yields [3].

Oxidative dehydrogenation of ethane (ODE) enables the cleavage of C-H bonds, resulting in almost commercially viable amounts of ethylene while maintaining high selectivity [4–6]. Moreover, carbon dioxide can

serve as a mild oxidizing agent in ODE [7–9]. This implies that an ODE process utilizing CO₂ (ODEC) not only enhances ethene production with remarkable selectivity but also contributes to reducing carbon emissions, thereby facilitating the achievement of carbon neutrality and addressing the global energy crisis [10,11]. Nevertheless, this process can only be initiated at critical reaction conditions, e.g., high reaction temperature and pressure [12]. Moreover, catalysts would be easily deactivated at harsh conditions owing to either sintering or coking [13]. Therefore, a green and sustainable catalytic approach to trigger ODEC at mild reaction requirements is highly desirable and remains challenging.

Photocatalysis seems to be an intriguing strategy for the ODEC process, while its light harvesting efficiency and throughput are impeded by the weak response ability, shallow depth of photon penetration, and fatigued dynamics of charge carriers of semiconductor-based photocatalysts [14–17]. Photothermal catalysis, integrating photochemical

* Corresponding authors.

E-mail addresses: chenhj@njtech.edu.cn (H. Chen), h.sun@ecu.edu.au (H. Sun), shaobin.wang@adelaide.edu.au (S. Wang).

<https://doi.org/10.1016/j.apcatb.2023.123166>

Received 22 March 2023; Received in revised form 29 May 2023; Accepted 10 August 2023

Available online 12 August 2023

0926-3373/© 2023 The Authors. Published by Elsevier B.V. This is an open access article under the CC BY-NC-ND license (<http://creativecommons.org/licenses/by-nc-nd/4.0/>).

and thermocatalytic processes into one unit, is deemed as a perfect solution to simultaneously reduce the energy consumption of thermocatalysis and increase the quantum efficiency of photocatalysis [18,19]. As a rising star in the past decade, photothermal catalysis has exhibited great potentials in the full-spectrum solar light harvesting for energy generation and fossil fuels upgrading [20–22]. Till now, it has already been demonstrated in versatile gas-solid-phase reactions, for examples, dry reforming of methane (DRM) [23], Fischer-Tropsch synthesis [24,25], Sabatier reaction [26–28], reverse water gas shift (RWGS) processes [29], and water splitting to H_2 [30,31]. Thus, photothermal catalysis with the participation of heat and energetic hot carriers (EHC) is placed great expectations on industrial feasibility to renovate conventional chemical industry technique and unit operations in a clean, safe and cost-effective manner [32]. To our knowledge, no such a work has been yet reported in ODEC to ethene.

Fe, Co and Ni non-noble metal loaded materials are typically thermocatalytic ODEC catalysts and exactly exhibit surface plasmon resonance (SPR) effects under light illumination for strong photo-to-electron/thermal abilities. In addition, carbonaceous materials can strongly absorb sunlight in a broad range from UV to IR, especially carbon nanotubes with the unique light confinement effect, thus are considered as ideal supports in photothermal catalysts. In this work, we synthesized carbon nanotubes (CNTs) confined non-noble bimetallic catalysts (FeNi@CNTs and CoNi@CNTs) for photothermal catalytic ODEC and illustrated the contributions of UV and visible bands to the reaction. Compared with graphene supported monometallic catalysts (Co/graphene, Fe/graphene, and Ni/graphene), the FeNi@CNTs bimetal catalyst exhibited an enhanced electric field and superior light-to-thermal efficiency. The resultant more EHC and heat on FeNi@CNTs collectively contributed to the highest ethene production rate and selectivity. More importantly, EHC excited under UV (EHC_{UV}) and visible light (420–490 nm, EHC_{VIS}) irradiations directly initiated ODEC and NODE, respectively, to produce ethene. While hot carriers induced under visible light (> 490 nm) failed to directly activate ethane and CO_2 and finally decayed into heat for thermocatalysis. Experiment and simulation results confirmed that thermocatalytic ODEC for ethene is preferred to thermocatalytic ethane cracking for methane on the fabricated FeNi@CNTs. Moreover, the photothermal effect turns more significant when solar light is brought into thermocatalytic ODEC (500 °C), increasing ethene evolution by one order of magnitude.

2. Experimental section

2.1. Catalyst preparation

FeNi@CNTs preparation. $K_4Fe(CN)_6 \cdot 3H_2O$ (2.5 mmol) was dissolved into 250 mL of ultra-pure water. Then, 100 mg urea derived carbon nitride nanosheets were dispersed with successive 1 h ultrasonication and 1 h stirring. After that, 250 mL of $NiSO_4 \cdot 6H_2O$ (0.01 M) was dropwise added by a peristaltic pump at a rate of 2 mL/min. FeNi Prussian blue analogue loaded carbon nitride was acquired after high speed centrifugation, several times of washing using water and alcohol and vacuum drying at 60 °C overnight. FeNi@CNTs was finally prepared by calcination of FeNi Prussian blue analogue/carbon nitride in N_2 at 500 °C for 2 h.

CoNi@CNTs preparation. The preparation process is similar to that of FeNi@CNTs except $K_4Fe(CN)_6 \cdot 3H_2O$ was substituted by $K_4Co(CN)_6 \cdot 3H_2O$.

Preparation of contrast samples. A certain amount of $FeCl_3 \cdot 3H_2O/Co(NO_3)_2 \cdot 6H_2O/Ni(NO_3)_2 \cdot 6H_2O$ was dissolved into 50 mL ultra-pure water, and then graphene was added with successive 1 h ultrasonication and 10 h stirring. A solid precursor was obtained by removal of water at 80 °C. Corresponding Fe/Co/Ni nanoparticle loaded graphene was finally acquired after H_2 reduction at 500 °C for 2 h.

2.2. Characterizations

The crystal structures of the prepared samples were analyzed with X-ray diffraction (XRD) on an X'Pert PRO MPD, Holland. The morphology was captured on a JEOL 2100. High-angle annular dark-field scanning transmission electron microscopy (HAADF-STEM) and energy-dispersive X-ray (EDX) elemental mapping images were recorded on a FEI Titan G2 80–200 TEM/STEM. X-ray photoelectron spectroscopy (XPS) was performed on a Kratos Axis Ultra DLD system under ultrahigh vacuum condition, and the results were calibrated with C 1 s reference signal (284.6 eV). Fourier transform infrared (FT-IR) spectra were collected on a PerkinElmer instrument. A Cary 100 UV-Vis spectrophotometer was used for recording the diffused reflectance spectra. Raman spectra were acquired by a DXR2 Raman Microscope (Thermo Fisher) with 532 nm line of Ar laser as the excitation source. XANES and EXAFS measurements were acquired at the wiggler X-ray absorption structure (XAS) beamline (12ID) at the Australian Synchrotron in Melbourne.

2.3. Evaluation of photothermal activity

The photothermal catalytic ODEC was carried out in a self-designed reactor equipped with an overhead Xenon lamp (See Fig. S1). At first, 20 mg catalyst was uniformly coated on a quartz microfiber filter. Before reaction, the catalyst was activated by H_2 at 500 °C for 1 h. After cooling down to ambient temperature, the reactor was flushed by Ar to evacuate the residual H_2 . Then the reaction gases ($C_2H_6/CO_2/Ar = 40/40/20$) were introduced into the reactor at a flow rate of 20 mL/min until the reactor was filled with the feed gases. The reaction was initiated by turning on the light (300–780 nm). In the meantime, a thermocouple under the catalyst bed was used to record the average temperature of catalysts during the reaction. The effluent gases were analyzed online by a gas chromatography (GC, Agilent 7820 A) equipped with Porapak N and Molsieve 5 A columns. The effect of light wavelength on photothermal catalytic ODEC performance was studied by changing light filters above 420 and 490 nm. Besides, thermocatalytic performance of FeNi@CNTs for ODEC and that under light irradiation were assessed by setting the furnace temperature at 500 °C. The carbon balance of the photothermal catalytic ODEC system is around 80 %. To study the photo-stability, we performed photothermal catalytic ODEC in a flow-type reaction at room temperature with light turning on and off. For observing the thermal stability, photothermal catalytic ODEC was performed in a flow-type reaction at 500 °C for three successive ethene monitoring.

2.4. Finite element method (FEM) simulation

In the FEM simulations, we used the COMSOL Multiphysics software [33] to elucidate the mechanism of the improved photothermal catalytic performance of the alloys-substrate composite under study. The FEM domain is filled with reagent. The catalysts were modelled to mimic their nanostructures. The radiation source is located at the top of the domain, transmitting downward vertically with an intensity of 10^4 W/m^2 . Following the experimental TEM images, the nanospheres of the alloys, made from FeNi and CoNi, are enclosed by the carbon nanotubes (CNT). In contrast, single element nanospheres of Fe, Co, and Ni are setting on the top of the graphene substrate, following the corresponding experimental setup. In this way, a comparison of the total heat generation can be made on the same benchmark. The optical parameters of the CNT [34], graphene, Fe, Co and Ni are adapted from previous works [35], while those for the CoNi and FeNi alloys are obtained from our DFT results using the CASTEP package [36]. In the DFT calculations, we used the plane wave basis set, together with the generalized gradient approximation (GGA) and Perdew-Burke-Ernzerhof (PBE) functional [37]. The cut off energy was defined to be 340 eV. The details of the DFT calculations may be found in our previous works [38,39].

2.5. Density functional theory (DFT) calculation

DFT calculations for mechanism investigations were carried out using the generalized gradient approximation (GGA) of Perdew Burke Ernzerhof (PBE) [37]. The Vienna ab initio simulation package (VASP) is used with the projected augmented-wave method. The kinetic cutoff energy for the plane-wave basis was set to be 400 eV. The Brillouin zone integration is conducted on a Γ -centered $3 \times 3 \times 1$ k mesh. All atoms are fully relaxed until the force on each atom is less than $0.03 \text{ eV } \text{\AA}^{-1}$.

3. Results and discussion

3.1. Catalyst synthesis and characterizations

The synthesis process of CNTs confined non-noble bimetallic alloys, i.e., FeNi@CNTs and CoNi@CNTs, includes two steps: an electrostatic self-assembly to load Prussian blue analogue (PBA) on 2-dimensional carbon nitride nanosheets, and subsequent calcination under inert atmosphere (Fig. 1). Specifically, regular FeNi or CoNi PBA nano-cubes were in situ grown on veil-like carbon nitride nanosheets derived from urea (Fig. S2). Then the obtained PBA/carbon nitride hybrids experienced a calcination process under N_2 . The calcination process underwent three stages, including collapse of PBA cubic nanostructure (Fig. S2a, d and g), pyrolysis of carbon nitride (Fig. S2b, e and h and S3) and orientated growth of carbon into CNTs confined bimetal alloy (Fig. S2c, f and i). After the calcination process, both FeNi@CNTs and CoNi@CNTs catalysts presented as nanoparticles encapsulated in bamboo-like CNTs (Fig. 2a-f). The lattice distances of metal nanoparticles in FeNi@CNTs and CoNi@CNTs catalysts are both 0.21 nm, stemming from the (111) crystal planes of FeNi and CoNi alloys (Fig. 2c and f) [40,41]. Meanwhile, the alloy nanoparticles were tightly enfolded with the carbon shells, as evidenced by the lattice distance of 0.34 nm [16].

The formation of CNTs confined bimetallic alloy nanostructures can also be proven by STEM-EDX mapping images. Fe-Ni and Co-Ni were evenly distributed in the FeNi and CoNi nanoparticles, respectively, which were surrounded by carbon (Fig. 2g-h and Figs. S4-S5). For comparisons, monometallic nanoparticles with the same metal loading to FeNi@CNTs and CoNi@CNTs catalysts (Fe: 20 %, Co: 20 % and Ni: 30 %, determined by ICP) were prepared by loading metals on graphene with an impregnation method (Fig. S6).

The crystal structure of the prepared samples was studied by X-ray diffraction (XRD) (Fig. 3a). A characteristic peak centered at roughly 26° can be found on all the samples, which originates from the carbon materials. Meanwhile, a peak at 44.28° can be observed on monometallic Ni/graphene and Co/graphene catalysts, attributing to the (111) planes of Ni and Co nanoparticles, respectively. No difference occurred for the (111) peak position between CoNi@CNTs and monometallic samples

[41]. Whilst FeNi@CNTs sample showed a slight downshift to 43.87° on the diffraction peak of the (111) plane as parts of Ni were replaced by Fe atoms with a smaller atomic radius, thus proving the formation of a FeNi alloy in the FeNi@CNTs catalyst.

X-ray photoelectron spectroscopy (XPS) was used for analysis of the surface chemical states of metals in the prepared samples (Fig. 3b and Fig. S7-12). The metallic state of Co (at 786.72 and 803.39 eV, Fig. S10), Fe (at 711 and 723.96 eV, Fig. S11), and Ni (at 861.59 and 880.08 eV, Fig. S12) can be found in the corresponding monometallic catalysts (Table S1). Metal oxides revealed in the XPS spectra are ascribed to the surface oxidation in air. Fe^0 , Co^0 and Ni^0 were also observed in CNTs encapsulated bimetallic catalysts, however, positive (positions of Fe^0 and Co^0) and negative (position of Ni^0) shifts were accompanied due to their modulated electronic structures. This further verified the formation of FeNi and CoNi bimetal alloys. In addition, Ni K-edge X-ray absorption near-edge structure (XANES) spectra and Fourier transform for the extended X-ray fine structure (EXAFS) measurements solidly confirmed the existence of FeNi bonding in FeNi@CNTs at a bond length of 2.2 \AA , rather than Fe-N coordination in PBA and Fe-Fe in Fe foil (Fig. 3c-d).

Moreover, Raman spectra displayed an obvious D band at $\sim 1351 \text{ cm}^{-1}$ and an apparent G band at $\sim 1593 \text{ cm}^{-1}$. The former D band belonged to the structural defects in the graphitic sp^2 network and the latter G band was assigned to the sp^2 hybridized carbon atoms in a hexagonal graphitic ring (Fig. 3e). The intensity ratio between the D and G bands (I_D/I_G) was almost the same between FeNi@CNTs and corresponding monometallic catalysts, suggesting a similar graphitization degree between CNTs shells of FeNi@CNTs and graphene. By contrast, a relatively low I_D/I_G ratio can be seen in CoNi@CNTs compared with graphene supported Co nanoparticles, which is possibly owing to the more pyrolic N doping realized by the pyrolyzation of carbon nitride (Fig. S3 and S9).

The light responsive ability of all the samples was studied. Compared with monometallic catalysts, CNTs confined bimetallic catalysts experienced sharp improvements in the absorption intensity throughout the whole solar light spectrum (Fig. 3f). This is because of the interaction within bimetallic alloy nanoparticles and the confinement effect of CNTs. Therefore, the enhanced light absorption would result in more hot carriers via Landau damping [42,43]. Hot carriers with higher energy than the HOMO/LUMO energies of reactants would directly participate in redox reactions in the form of EHC. While hot carriers failed to reduce/oxidize reactants would activate reactants and accelerate the reaction rate by decaying into heat via Ohmic damping. Both EHC and heat are two important components in the photothermal catalytic process.

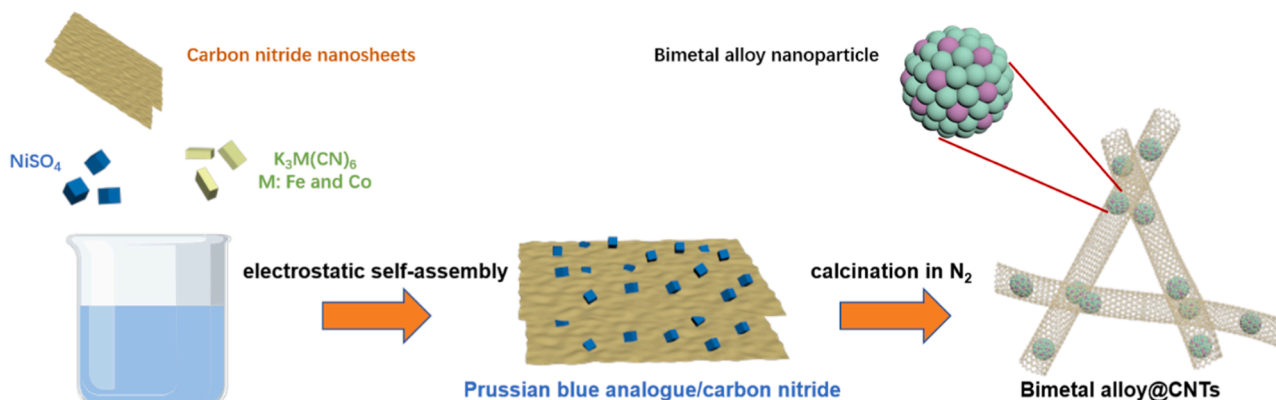


Fig. 1. Illustration of synthesis of carbon nanotubes confined bimetallic alloy photothermal catalysts.

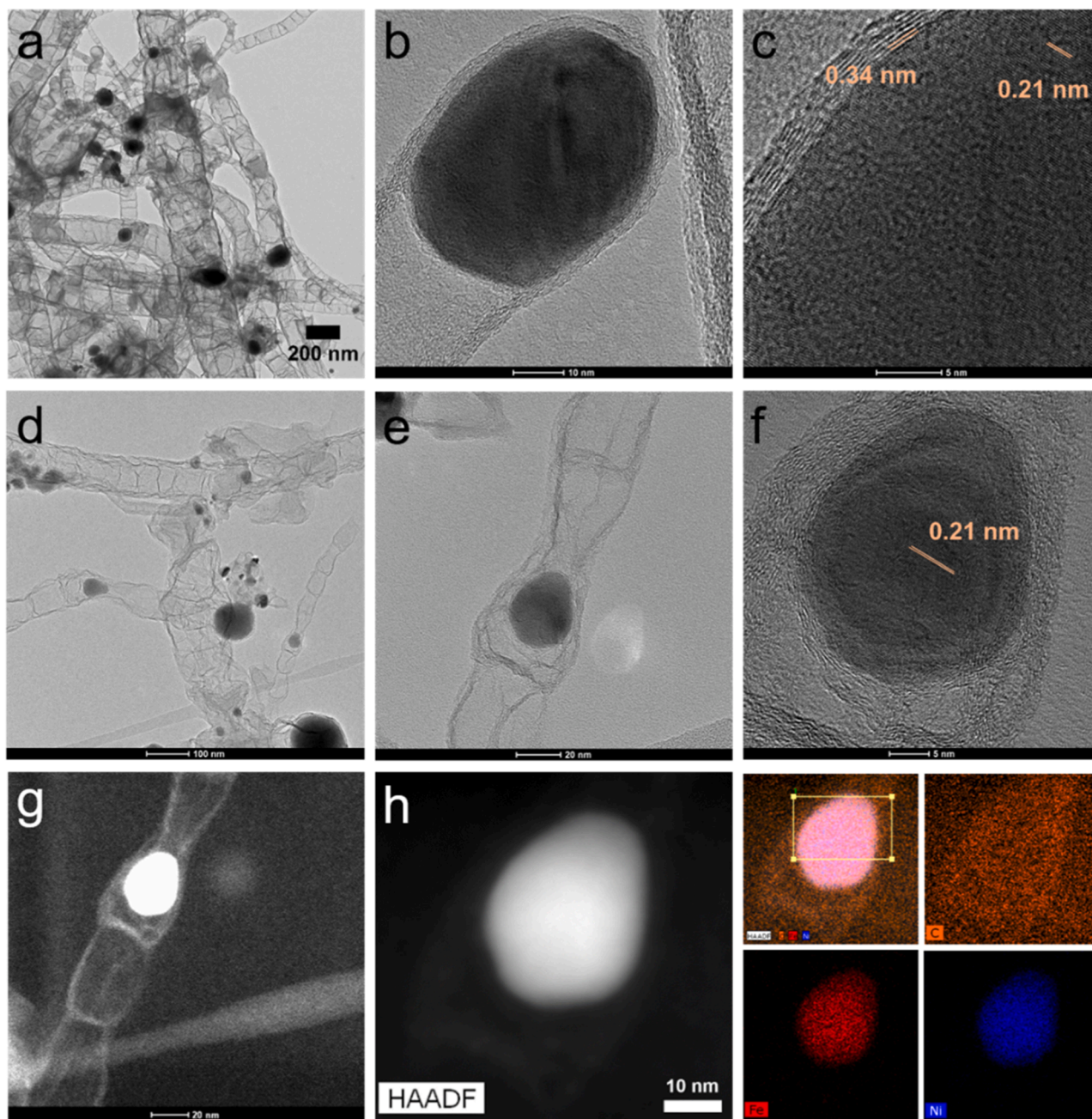


Fig. 2. Catalyst characterizations. (a-c) Transmission electron microscope (TEM) images of CoNi@CNTs. (d-f) TEM images of FeNi@CNTs. (g, h) High-angle annular dark field (HAADF) and elemental mapping images of FeNi@CNTs.

3.2. Photothermal catalytic activity

Photothermal catalytic ODEC to ethene was carried out in a self-designed fixed-bed quartz reactor with a continuous gas flow at atmospheric pressure (Fig. S1). The reactor allows all the feed gas to pass through the catalyst bed. A passband infrared (IR) filter was used on the Xenon lamp to avoid the thermal effect of IR light on the surface of the catalysts. The thermal energy in the photothermal catalysis only comes from the conversion of UV and visible lights to heat in the absence of external heating. Prior to reaction, a blank photothermal catalytic experiment in the absence of a catalyst was performed, and no product can be detected, proving the reliability of the self-designed reactor. Meanwhile, carbonaceous materials including graphene and carbon nanotube were used for photothermal ODEC but no CO gas was detected, proving that the carbonaceous supports cannot react with reactants

for C-based products.

The photothermal catalytic activities of all the catalysts in the ODEC process were evaluated. Simultaneously, the catalyst temperature was in situ monitored by a thermocouple during the reaction process. Although this measurement may not provide an exact reading of the catalyst surface temperature, it can still be utilized to comparatively assess the solar-to-thermal conversion efficiency among different catalysts in this study [44]. The average temperature of all the catalysts stabilized above 150 °C after 1 h light irradiation, especially FeNi@CNTs reached the highest at about 200 °C, suggesting their remarkable photo-to-thermal capabilities (Fig. 4a). Compared with the light absorption ability of catalysts in an order: CoNi@CNTs > FeNi@CNTs > Co/graphene > Fe/graphene > Ni/graphene (Fig. 3f), catalyst temperature showed a different order in FeNi@CNTs > CoNi@CNTs > Fe/graphene > Ni/graphene > Co/graphene. The difference reflects that Fe exhibits higher

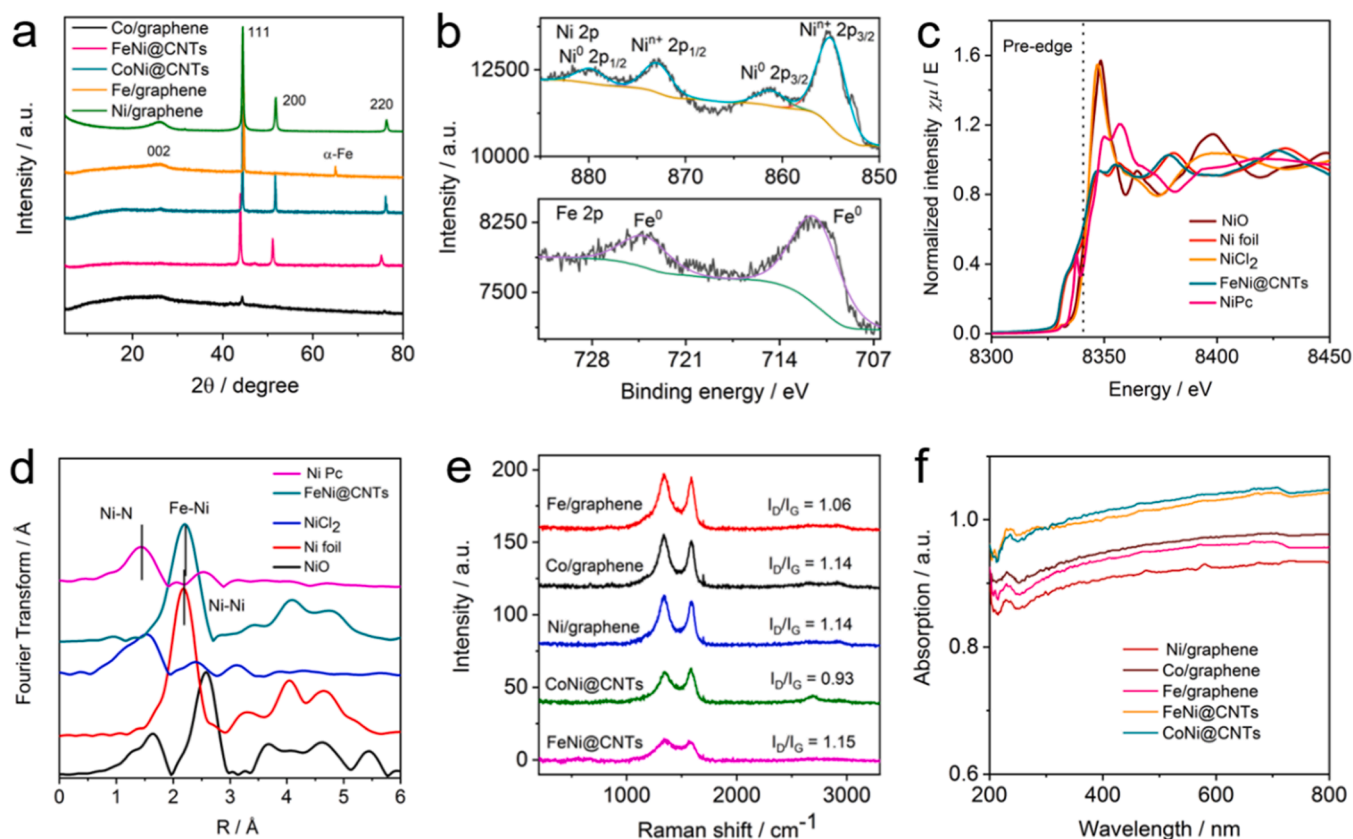


Fig. 3. Catalyst structure investigations. (a) XRD patterns of different samples. (b) Fe 2p and Ni 2p XPS spectra of FeNi@CNTs. (c) Ni K-edge X-ray absorption near-edge structure (XANES) spectra. (d) Fourier transform for the extended X-ray fine structure (EXAFS) measurements of FeNi@CNTs and standard references. (e) Raman spectra, and (f) UV-Vis spectra of all the prepared samples.

photo-to-thermal efficiency than Co, rendering FeNi bimetallic catalyst with more heat generated than CoNi bimetallic catalyst. Additionally, the temperatures of graphene and carbon nanotubes were monitored both in situ (Fig. S13) and ex situ (Fig. S14) under light irradiation. The results indicate a higher temperature on carbon nanotubes than graphene, confirming the confinement effect on light absorption and photo-to-thermal efficiency.

In the photothermal ODEC process, C₂H₄ and syngas are the main products on all the metallic catalysts (Table 1). Methane can simultaneously be detected as a byproduct owing to the ethane cracking process. Apart from a high photothermal catalytic performance of ODEC to ethene, Ni/graphene showed superior photothermal catalytic abilities of ethane cracking and ethane dry reforming, especially an extremely high yield of CO (111,055 $\mu\text{mol/h/g}$). As thus, the selectivity of ethene in the effluent products is much low at 1.1 % despite of a high ethane conversion of 2.6 %. Co/graphene shows worse activities in photothermal catalytic ethane conversion compared with Ni/graphene and a low selectivity to ethene. Consequently, the ethene selectivity is not improved for CoNi bimetallic nanoparticles in the pore channels of CNTs. While mono-Fe based catalyst behaved the best selectivity to ethene among the three monometallic catalysts regardless of low activations of ethane and CO₂. The C₂H₄ evolution rate stood out in all the samples after encapsulating FeNi bimetallic nanoparticles into CNTs, reaching as high as 768 $\mu\text{mol/h/g}$ (Fig. 4b). In the meantime, the processes of ethane cracking and ethane dry reforming are significantly suppressed, enabling the selectivity of C₂H₄ in the effluents for FeNi@CNTs reaches as high as 44.7 %.

It should be mentioned that the photothermal catalytic performance of FeNi@CNTs in ODEC is comparable to its thermocatalytic activity at 500 °C (Table 1) and higher than photocatalysis with noble metals loaded semiconductor-based catalysts (Table S2). Besides, the photo-

stability of FeNi@CNTs was investigated by turning light on and off in photothermal catalytic ODEC. A reproducibility was observed after the light was on again, meaning a good stability of FeNi@CNTs (Fig. 4c). Furthermore, the catalyst maintained stable properties after the photothermal catalysis as revealed by the unchanged XRD peaks, XPS results and I_D/I_G ratio (Fig. S15–20). Considering the mild reaction conditions (atmospheric pressure) and less energy consumptions (without external heating), the results in this photothermal catalytic system proves that the photons contribute significantly to offsetting the endotherm of ODEC, showing a great improvement in environment and process efficiency.

3.3. Contributions of light wavelength bands

To unveil the photo effect on photothermal catalytic ODEC, we tested light with different wavelength bands for ethane and CO₂ activations (Fig. 4d). When the light was changed from UV+Vis to visible light only, product of CO disappeared in the effluent. UV light has enough energy for the excitation of EHC compared with visible light, as such, the energetic hot electrons induced by UV light rather than visible light in the photothermal catalytic system are responsible for the reduction of CO₂. Ethene evolution rate is sharply decreased from 768 to 158 $\mu\text{mol/h/g}$ when UV light was filtered off. Instead, methane generation rate keeps unchanged, suggesting that energetic hot holes excited by UV light is mainly involved into the cleavage of C-H bond in ethane to ethene (Fig. 4e). Moreover, the ethene production rate dropped while methane generation rate remained when visible light at a specific range of 420–490 nm was further cut, indicating that EHC_{vis} at a shorter wavelength range (420–490 nm) are in charge of NODE to ethene and hydrogen (Fig. 4e). This is because the hot electrons excited under visible light (420–490 nm) are less energetic than that induced by UV

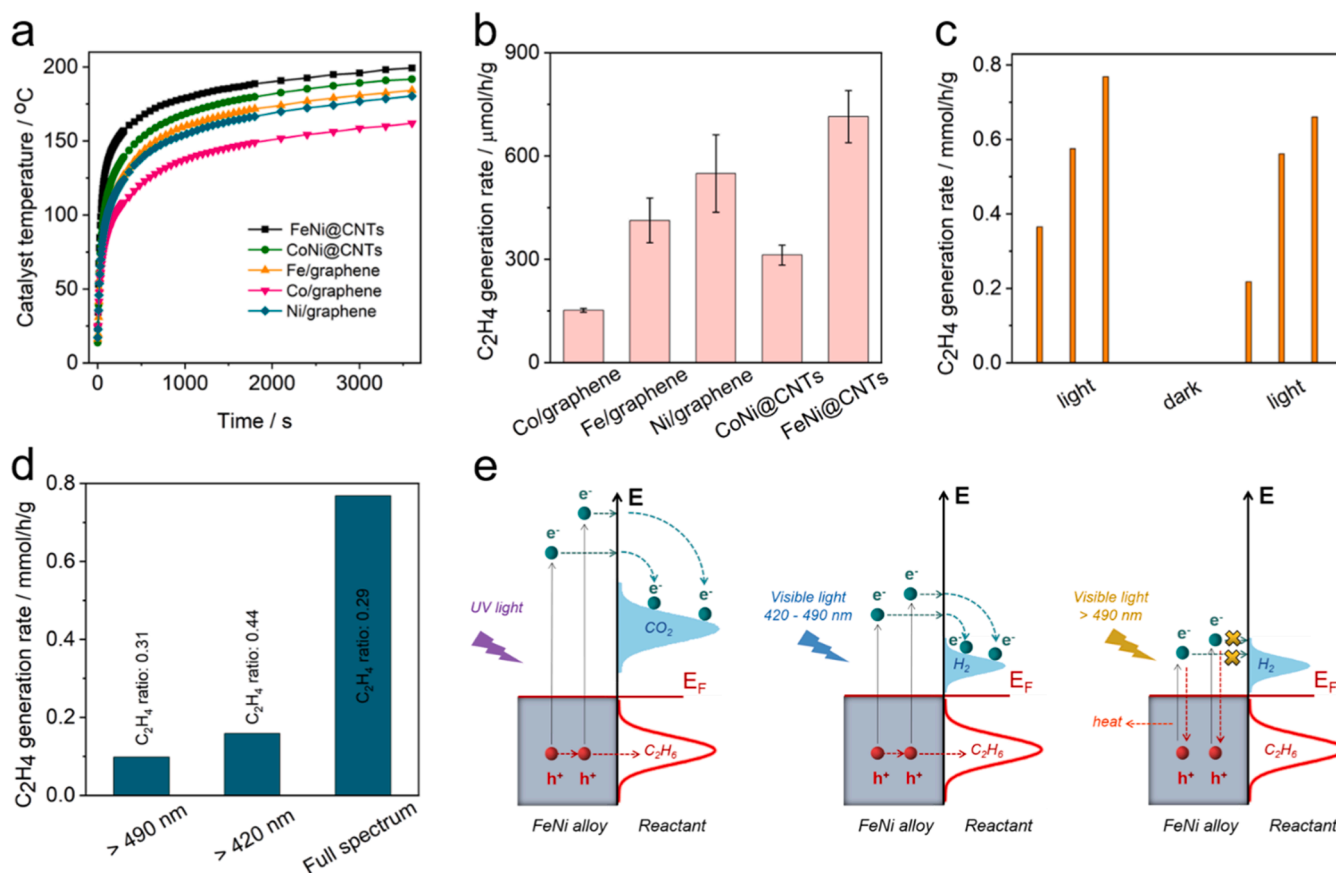


Fig. 4. Performance evaluations. (a) Catalyst temperatures monitored during photothermal catalytic ODEC. (b) Photothermal catalytic performances of ODEC on various catalysts. (c) Photothermal catalytic ODEC with light on and off. (d) Effect of light band on the photothermal catalytic ODEC. (e) Photothermal effects in photothermal catalysis.

Table 1
Photothermal ODEC performances of the as-prepared samples.

Performance Sample	CH ₄ μmol/h/g	H ₂ μmol/h/g	CO μmol/h/g	C ₂ H ₄ μmol/h/g	C ₂ H ₆ conversion %	^a S _{C₂H₄} %
Ni/graphene	614	23517	111055	629	2.6	1.1
Co/graphene	222	370	7096	148	0.4	3.9
Fe/graphene	223	321	1656	459	0.3	32.8
CoNi@CNTs	214	978	17911	292	1.1	3.1
^b FeNi@CNTs	220	45	1682	768	0.4	44.7
^c FeNi@CNTs	210	12	NA	98	NA	48.3
^d FeNi@CNTs	202	16	NA	158	NA	61.0
^e FeNi@CNTs	236	171	4321	1767	0.5	43.7
^f FeNi@CNTs	389	986	24759	8952	2.3	41.6

^a C₂H₄ selectivity S_{C₂H₄} = C₂H₄ generation rate / (C₂H₄ generation rate + 1/2 CO generation rate + 1/2 CH₄ generation rate).

^b Photothermal ODEC under full spectrum light irradiation;

^c Photothermal ODEC under irradiation of light above 490 nm;

^d Photothermal ODEC under irradiation of light above 420 nm;

^e Thermocatalytic ODEC at furnace temperature of 500 °C;

^f Photothermal catalytic ODEC at furnace temperature of 500 °C;

light. Therefore, the hot electrons can only realize the H₂ production, rather than CO₂ reduction (Fig. 4e). Visible light at a longer wavelength range (> 490 nm) unselectively triggers ethane cracking for methane and dehydrogenation of ethane to ethene. The trend is consistent with thermocatalysis, indicating hot carriers excited by visible light at above 490 nm fail to activate the reactants and finally participate in photothermal catalysis in the form of heat (Fig. 4e). Based on this, the selectivity for different catalytic pathways (ODEC, NODE, ethane cracking

and ethane reforming processes) can be regulated via changing the wavelength bands of solar light.

The photothermal effects with different light wavelength bands in photothermal catalytic ODEC can be explained by the monitored catalyst temperature (Fig. S21). The catalyst temperature reached as high as 209 °C under UV+visible light illumination and stabilized at 202 and 190 °C after UV light and UV+visible light (420–490 nm) are filtered, respectively. This suggests that most hot carriers excited by UV+visible light (420–490 nm) are energetic enough to directly activate reactants, while most hot carriers excited by visible light (> 490 nm) decay into heat.

3.4. Mechanistic investigations

Photothermal catalysis is integrated by an energetic hot carriers-driven photochemical process and a thermocatalysis actuated by the heat from decay of hot carriers. As such, to explain the high generation rate and selectivity to ethene on FeNi@CNTs in photothermal catalysis, we first conducted simulations of enhanced electric field and generated heat under light illumination with the finite element method (FEM) (Fig. 5a, b and Fig. S22–25). Fe/graphene exhibits a higher electric field than Ni/graphene catalyst only in part of UV spectrum. An electric field would be generated in the form of free movement of hot electrons. As such, the stronger intensity of the electric field suggests higher density of high-energy electrons. Considering the stronger C-H bond (423 kJ/mol) than C-C bond (377 kJ/mol), EHC_{UV} are thermodynamically more favorable for the cleavage of the C-H bond of ethane. Therefore, a higher selectivity for ethene generation is realized on Fe/graphene than on Ni/graphene. After the fabrication of FeNi@CNTs, the electric field is remarkably enhanced throughout UV+Vis light regions. Especially, the

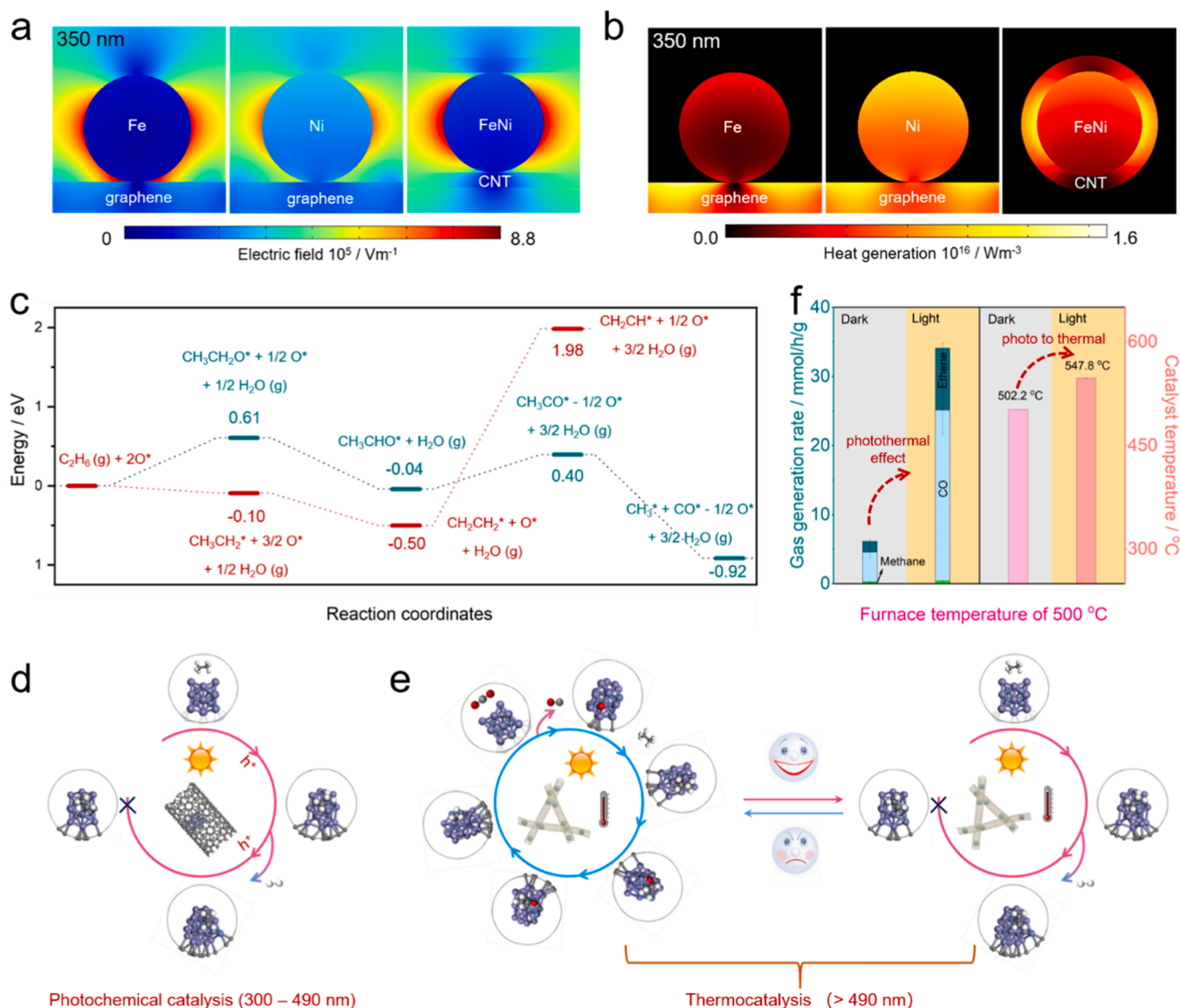


Fig. 5. Mechanism investigations. (a) FEM simulations of electric field of FeNi@CNTs, Fe/graphene and Ni/graphene, (b) FEM simulations of generated heat on different configurations of photothermal catalysts, (c) DFT simulations of reaction energy for ODEC and ethane cracking processes, (d-e) reaction mechanism and pathways of photothermal catalytic ODEC process with FeNi@CNTs and (f) photothermal effect when light is introduced into thermocatalytic (500 °C).

electric field under UV light is higher than that under visible light. Therefore, more EHCs are excited on FeNi@CNTs than graphene supported monometallic catalysts, which are beneficial for the dissociation of CO_2 and cleavage of C-H bond.

Besides, more heat is generated on the bimetal alloy in the confined pore channels, as shown from Fig. 5b and Fig. S24–25. This is consistent with the highest catalyst temperature of FeNi@CNTs in photothermal catalysis (Fig. 4a). For the photo-converted heat driven thermocatalytic process in photothermal catalysis, density functional theory (DFT) calculation is then performed to investigate the thermocatalytic pathways on FeNi@CNTs for the breakup of C-H bond of ethane to ethene and dissociation of C-C bond of ethane to methane/syngas (Fig. S26–27).

As displayed in Fig. 5c and Table S3, the C-H bond cleavage along the oxidative dehydrogenation reaction $C_2H_6(g) + 2O^* \rightarrow CH_3CH_2^* + 3/2 O^* + 1/2 H_2O(g)$ ($\Delta E = -0.1$ eV) pathway is thermodynamically and kinetically more favorable than the O^* insertion reaction $C_2H_6(g) + 2O^* \rightarrow CH_3CH_2O^* + 1/2 O^* + 1/2 H_2O(g)$ ($\Delta E = 0.61$ eV). This is the main reason for the high selectivity for ethene on FeNi@CNTs in thermocatalysis. The formed $CH_3CH_2O^*$ undergoes two facile

dehydrogenation reactions: $CH_3CH_2O^* + 1/2 O^* + 1/2 H_2O(g) \rightarrow CH_3CHO^* + H_2O(g)$ and $CH_3CHO^* + H_2O(g) \rightarrow CH_3CO^* - 1/2 O^* + 3/2 H_2O(g)$ to produce CH_3CO^* , which facilitates the C-C bond cleavage to form $CH_3^* + CO^*$. The C-C bond cleavage via $CH_3CH_2O^*$ and CH_3CO^* intermediates shows that the oxidative C-C bond cleavage is preferred on the top-top site of FeNi alloy (Table S4). While the formed $CH_3CH_2^*$ experienced a further dehydrogenation process to ethene: $CH_3CH_2^* + 3/2 O^* + 1/2 H_2O(g) \rightarrow CH_2CH_2^* + O^* + H_2O(g)$. After that, it is difficult to break C-H bond of the formed ethene ($CH_2CH_2^* + O^* + H_2O(g) \rightarrow CH_2CH_2^* + 1/2 O^* + 3/2 H_2O(g)$) owing to the high reaction energy of 2.48 eV, so that ethene is easy to be emitted as the final product in the C-H bond cleavage pathway. Therefore, the DFT results confirmed that ODEC to ethene is also preferred on FeNi@CNTs catalyst in thermocatalysis driven by photo generated heat. As the results, these two enhanced components of EHC and heat render FeNi@CNTs higher performance and selectivity for ODEC to ethene in photothermal catalysis.

The reaction mechanism for photothermal catalytic ODEC on FeNi@CNTs is summarized based on the EHC driven photochemical

catalysis and internal thermal induced thermocatalysis. EHC_{UV} and EHC_{VIS} (420–490 nm) directly initiate ODEC and NODE, respectively to ethene (Fig. 5d). While hot carriers induced by visible light (> 490 nm) failing to activate CO_2 and ethane molecules will decay in the form of heat. Ethene is the main product on FeNi@CNTs in photo induced thermocatalysis, attributing to the lower reaction energy of C-H bond cleavage than C-C bond dissociation (Fig. 5e). Therefore, the enhanced electric field and the reduced thermodynamic reaction energy for C-H bond cleavage on FeNi@CNTs contribute the high selectivity for ethene.

3.5. Scale up of photothermal effect

Photothermal effect was introduced into a flow-type thermocatalytic ODEC process (external heating of 500 °C) with FeNi@CNTs. Compared with thermocatalytic performance, photothermal catalysis exhibits a remarkable enhancement on the generation of ethene (9.0 mmol/h/g) and a good stability in three successive ethene monitoring (Fig. 5f and Fig. S28). The photothermal effect at 500 °C is calculated by subtracting the thermocatalytic performance from photothermal catalytic performance (Table 1). The photothermal effect at 500 °C on ethene evolution rate (7.2 mmol/h/g) is extraordinarily improved by an order of magnitude than that without external heating. Meanwhile, the selectivity for ethene remains as high as 41.6 % after thermocatalytic ODEC is irradiated by solar light. The enhanced performance is attributed to the more energetic hot carriers at external heating and the more heat of 45 °C of temperature increase on FeNi@CNTs under light irradiation. Considering the external heat can be derived from solar light (infrared light heating or light concentrator), ODEC to ethene will be realized in a clean and sustainable manner.

4. Conclusions

Bimetallic alloys encapsulated by CNTs have been derived from Prussian blue analogues/ C_3N_4 precursors. The fabricated FeNi bimetallic alloy with CNTs confinement behaves an enhanced electric field compared with its monometallic catalyst counterparts, leading to more EHC and internal heat. The EHC_{UV} and EHC_{VIS} (420–490 nm) directly initiate ODEC and NODE, respectively, to ethene. While hot carriers excited by visible light (> 490 nm) are responsible for internal heat. The resultant thermocatalysis is favorable for the cleavage of C-H bond of ethane to ethene. As such, the enhanced electric field for more hot carriers and the reduced thermodynamic reaction energy for C-H bond cleavage on FeNi@CNTs collectively achieve a higher production rate and selectivity for ethene. The photothermal effect on ethene evolution and selectivity is dramatically enhanced when solar light is introduced into thermocatalysis. This work unravels the key components and their roles in photothermal catalysis and provides a sustainable strategy for ethane and CO_2 conversions, as well as ethene production.

CRedit authorship contribution statement

Jinqiang Zhang: Conceptualization, Methodology, Data curation, Writing - original draft. **Meng Li:** Software, Investigation. **Xiaojie Tan:** Software, Investigation. **Lei Shi:** Data curation. **Kun Xie:** Conceptualization, Resources. **Xiaoli Zhao:** Software, Investigation. **Shuaijun Wang:** Methodology. **Shiyong Zhao:** Methodology. **Huayang Zhang:** Methodology. **Xiaoguang Duan:** Methodology. **Haijun Chen:** Resources, Funding acquisition, Supervision. **Yuezhao Zhu:** Resources, Conceptualization. **Mingbo Wu:** Resources, Conceptualization. **Hongqi Sun:** Funding acquisition, Data curation, Supervision. **Shaobin Wang:** Project administration, Funding acquisition, Writing - review & editing, Supervision.

Declaration of Competing Interest

The authors declare that they have no known competing financial

interests or personal relationships that could have appeared to influence the work reported in this paper.

Data availability

Data will be made available on request.

Acknowledgements

The author (H. Sun) would like to thank the support from ECU Vice-Chancellor's Professorial Research Fellowship. The support from the National Natural Science Foundation of China (51676096) is acknowledged. This work is also partially supported by the Australian Research Council (DP200103206 and DP190103548) and the scientific and technological innovation project of carbon emission peak and carbon neutrality of Jiangsu Province (No. BE2022024).

Appendix A. Supporting information

Supplementary data associated with this article can be found in the online version at doi:10.1016/j.apcatb.2023.123166.

References

- [1] Z. Yang, H. Li, H. Zhou, L. Wang, L. Wang, Q. Zhu, J. Xiao, X. Meng, J. Chen, F. S. Xiao, Coking-resistant iron catalyst in ethane dehydrogenation achieved through siliceous zeolite modulation, *J. Am. Chem. Soc.* 142 (2020) 16429–16436, <https://doi.org/10.1021/jacs.0c07792>.
- [2] S. Najari, S. Saeidi, P. Concepcion, D.D. Dionysiou, S.K. Bhargava, A.F. Lee, K. Wilson, Oxidative dehydrogenation of ethane: catalytic and mechanistic aspects and future trends, *Chem. Soc. Rev.* 50 (2021) 4564–4605, <https://doi.org/10.1039/D0CS01518K>.
- [3] B. Yan, S. Yao, S. Kattel, Q. Wu, Z. Xie, E. Gomez, P. Liu, D. Su, J.G. Chen, Active sites for tandem reactions of CO_2 reduction and ethane dehydrogenation, *Proc. Natl. Acad. Sci.* 115 (2018) 8278–8283, <https://doi.org/10.1073/pnas.1806950115>.
- [4] H.J. Dar, H.A. Jakobsen, K.R. Rout, K.J. Jens, D. Chen, Autothermal gas-phase oxidative dehydrogenation of ethane to ethylene at atmospheric pressure, *Ind. Eng. Chem. Res.* 60 (2021) 6784–6802, <https://doi.org/10.1021/acs.iecr.1c00678>.
- [5] C.A. Gärtner, A.C. van Veen, J.A. Lercher, Oxidative dehydrogenation of ethane: common principles and mechanistic aspects, *ChemCatChem* 5 (2013) 3196–3217, <https://doi.org/10.1002/cctc.201200966>.
- [6] J.L. Park, S.K. Balijepalli, M.D. Argyle, K.J. Stowers, Low temperature oxidative dehydrogenation of ethane by Ce-modified NiNb catalysts, *Ind. Eng. Chem. Res.* 57 (2018) 5234–5240, <https://doi.org/10.1021/acs.iecr.8b00531>.
- [7] M. Myint, B. Yan, J. Wan, S. Zhao, J.G. Chen, Reforming and oxidative dehydrogenation of ethane with CO_2 as a soft oxidant over bimetallic catalysts, *J. Catal.* 343 (2016) 168–177, <https://doi.org/10.1016/j.jcat.2016.02.004>.
- [8] S.B. Wang, K. Murata, T. Hayakawa, S. Hamakawa, K. Suzuki, Dehydrogenation of ethane with carbon dioxide over supported chromium oxide catalysts, *Appl. Catal. A: Gen.* 196 (2000) 1–8, [https://doi.org/10.1016/S0926-860X\(99\)00450-0](https://doi.org/10.1016/S0926-860X(99)00450-0).
- [9] S.B. Wang, Z.H. Zhu, Catalytic conversion of alkanes to olefins by carbon dioxide oxidative dehydrogenations: a review, *Energy Fuels* 18 (2004) 1126–1139, <https://doi.org/10.1021/ef0340716>.
- [10] M. Numan, E. Eom, A. Li, M. Mazur, H.W. Cha, H.C. Ham, C. Jo, S.-E. Park, Oxidative dehydrogenation of ethane with CO_2 as a soft oxidant over a PtCe bimetallic catalyst, *ACS Catal.* 11 (2021) 9221–9232, <https://doi.org/10.1021/acscatal.1c01156>.
- [11] Y. Song, L. Lin, W. Feng, X. Zhang, Q. Dong, X. Li, H. Lv, Q. Liu, F. Yang, Z. Liu, G. Wang, X. Bao, Interfacial enhancement by $\gamma\text{-Al}_2\text{O}_3$ of electrochemical oxidative dehydrogenation of ethane to ethylene in solid oxide electrolysis cells, *Angew. Chem. Int. Ed.* 58 (2019) 16043–16046, <https://doi.org/10.1002/anie.201908388>.
- [12] Z. Xie, D. Tian, M. Xie, S.Z. Yang, Y. Xu, N. Rui, J.H. Lee, S.D. Senanayake, K. Li, H. Wang, S. Kattel, J.G. Chen, Interfacial active sites for CO_2 assisted selective cleavage of C-C/C-H bonds in ethane, *Chem* 6 (2020) 2703–2716, <https://doi.org/10.1016/j.chempr.2020.07.011>.
- [13] J. Lu, B. Fu, M.C. Kung, G. Xiao, J.W. Elam, H.H. Kung, P.C. Stair, Coking- and sintering-resistant palladium catalysts achieved through atomic layer deposition, *Science* 335 (2012) 1205–1208, <https://doi.org/10.1126/science.1212906>.
- [14] R. Zhang, H. Wang, S. Tang, C. Liu, F. Dong, H. Yue, B. Liang, Photocatalytic oxidative dehydrogenation of ethane using CO_2 as a soft oxidant over Pd/TiO₂ catalysts to C_2H_4 and syngas, *ACS Catal.* 8 (2018) 9280–9286, <https://doi.org/10.1021/acscatal.8b02441>.
- [15] J. Zhang, X. Zhao, L. Chen, S. Li, H. Chen, Y. Zhu, S. Wang, Y. Liu, H. Zhang, X. Duan, M. Wu, S. Wang, H. Sun, Intrinsic mechanisms of morphological engineering and carbon doping for improved photocatalysis of 2D/2D carbon nitride van der Waals heterojunction, *Energy Environ. Mater.* (2022), <https://doi.org/10.1002/eeem2.12365>.

- [16] J. Zhang, Y. Li, X. Zhao, H. Zhang, L. Wang, H. Chen, S. Wang, X. Xu, L. Shi, L. C. Zhang, J.P. Veder, S. Zhao, G. Nealon, M. Wu, S. Wang, H. Sun, A hydrogen-initiated chemical epitaxial growth strategy for in-plane heterostructured photocatalyst, *ACS Nano* 14 (2020) 17505–17514, <https://doi.org/10.1021/acsnano.0c07934>.
- [17] Q. Li, H. Yue, C. Liu, K. Ma, S. Zhong, B. Liang, S. Tang, A photocatalytic transformation realized by Pd/TiO₂ particle size modulation: from oxidative dehydrogenation of ethane to direct dehydrogenation of ethane, *Chem. Eng. J.* 395 (2020), 125120, <https://doi.org/10.1016/j.cej.2020.125120>.
- [18] D. Mateo, J.L. Cerrillo, S. Durini, J. Gascon, Fundamentals and applications of photo-thermal catalysis, *Chem. Soc. Rev.* 50 (2021) 2173–2210, <https://doi.org/10.1039/D0CS00357C>.
- [19] M. Ghossoub, M. Xia, P.N. Duchesne, D. Segal, G. Ozin, Principles of photothermal gas-phase heterogeneous CO₂ catalysis, *Energy Environ. Sci.* 12 (2019) 1122–1142, <https://doi.org/10.1039/C8EE02790K>.
- [20] J. Zhang, L. Wang, X. Zhao, L. Shi, H. Chen, S. Zhang, P. Zhang, S. Wang, L. C. Zhang, Y. Wang, X. Wang, Y. Zhu, H. Zhang, X. Duan, M. Wu, G. Shao, S. Wang, H. Sun, The nature of active sites for plasmon-mediated photothermal catalysis and heat coupled photocatalysis in dry reforming of methane, *Energy Environ. Mater.* (2022), <https://doi.org/10.1002/eeem.2.12416>.
- [21] J. Zhang, Y. Li, J. Sun, H. Chen, Y. Zhu, X. Zhao, L.-C. Zhang, S. Wang, H. Zhang, X. Duan, L. Shi, S. Zhang, P. Zhang, G. Shao, M. Wu, S. Wang, H. Sun, Regulation of energetic hot carriers on Pt/TiO₂ with thermal energy for photothermal catalysis, *Appl. Catal. B: Environ.* 309 (2022), 121263, <https://doi.org/10.1016/j.apcatb.2022.121263>.
- [22] B. Han, W. Wei, L. Chang, P. Cheng, Y.H. Hu, Efficient visible light photocatalytic CO₂ reforming of CH₄, *ACS Catal.* 6 (2015) 494–497, <https://doi.org/10.1021/acscatal.5b02653>.
- [23] H. Liu, X. Meng, T.D. Dao, H. Zhang, P. Li, K. Chang, T. Wang, M. Li, T. Nagao, J. Ye, Conversion of carbon dioxide by methane reforming under visible-light irradiation: surface-plasmon-mediated nonpolar molecule activation, *Angew. Chem. Int. Ed.* 54 (2015) 11545–11549, <https://doi.org/10.1002/anie.201504933>.
- [24] X.N. Guo, Z.-F. Jiao, G.Q. Jin, X.-Y. Guo, Photocatalytic Fischer-Tropsch synthesis on graphene-supported worm-like ruthenium nanostructures, *ACS Catal.* 5 (2015) 3836–3840, <https://doi.org/10.1021/acscatal.5b00697>.
- [25] Z. Li, J. Liu, Y. Zhao, G.I.N. Waterhouse, G. Chen, R. Shi, X. Zhang, X. Liu, Y. Wei, X.D. Wen, L.Z. Wu, C.H. Tung, T. Zhang, Co-based catalysts derived from layered-double-hydroxide nanosheets for the photothermal production of light olefins, *Adv. Mater.* 30 (2018), e1800527, <https://doi.org/10.1002/adma.201800527>.
- [26] X. Meng, T. Wang, L. Liu, S. Ouyang, P. Li, H. Hu, T. Kako, H. Iwai, A. Tanaka, J. Ye, Photothermal conversion of CO₂ into CH₄ with H₂ over Group VIII nanocatalysts: an alternative approach for solar fuel production, *Angew. Chem. Int. Ed.* 53 (2014) 11478–11482, <https://doi.org/10.1002/ange.201404953>.
- [27] P.G. O'Brien, A. Sandhel, T.E. Wood, A.A. Jelle, L.B. Hoch, D.D. Perovic, C. A. Mims, G.A. Ozin, Photomethanation of gaseous CO₂ over Ru/silicon nanowire catalysts with visible and near-infrared photons, *Adv. Sci.* 1 (2014), 1400001, <https://doi.org/10.1002/advs.201400001>.
- [28] X. Zhang, X. Li, D. Zhang, N.Q. Su, W. Yang, H.O. Everitt, J. Liu, Product selectivity in plasmonic photocatalysis for carbon dioxide hydrogenation, *Nat. Commun.* 8 (2017), 14542, <https://doi.org/10.1038/ncomms14542>.
- [29] L.B. Hoch, P.G. O'Brien, A. Jelle, A. Sandhel, D.D. Perovic, C.A. Mims, G.A. Ozin, Nanostructured indium oxide coated silicon nanowire arrays: a hybrid photothermal/photochemical approach to solar fuels, *ACS Nano* 10 (2016) 9017–9025, <https://doi.org/10.1021/acsnano.6b05416>.
- [30] X. Li, J. Lin, J. Li, H. Zhang, X. Duan, H. Sun, Y. Huang, Y. Fang, S. Wang, Temperature-induced variations in photocatalyst properties and photocatalytic hydrogen evolution: differences in UV, visible, and infrared radiation, *ACS Sustain. Chem. Eng.* 9 (2021) 7277–7285, <https://doi.org/10.1021/acssuschemeng.1c01262>.
- [31] X. Li, S. Zhao, X. Duan, H. Zhang, S.-z Yang, P. Zhang, S.P. Jiang, S. Liu, H. Sun, S. Wang, Coupling hydrothermal and photothermal single-atom catalysis toward excellent water splitting to hydrogen, *Appl. Catal. B: Environ.* 283 (2021), 119660, <https://doi.org/10.1016/j.apcatb.2020.119660>.
- [32] L. Zhou, D.F. Swearer, C. Zhang, H. Robotzaji, H. Zhao, L. Henderson, L. Dong, P. Christopher, E.A. Carter, P. Nordlander, N.J. Halas, Quantifying hot carrier and thermal contributions in plasmonic photocatalysis, *Science* (2018) 69–72, <https://doi.org/10.1126/science.aat6967>.
- [33] R.W. Pryor, *Multiphysics modeling using COMSOL: a first principles approach*, Jones & Bartlett Publishers, 2009.
- [34] W.A. DeHeer, W. Bacsá, A. Chatelain, T. Gerfin, R. Humphrey-Baker, L. Forro, D. Ugarte, Aligned carbon nanotube films: production and optical and electronic properties, *Science* 268 (1995) 845–847, <https://doi.org/10.1126/science.268.5212.845>.
- [35] E.D. Palik, *Handbook of optical constants of solids*, Academic, Orlando, 1985, pp. 286–297.
- [36] S.J. Clark, M.D. Segall, C.J. Pickard, P.J. Hasnip, M.I. Probert, K. Refson, M. C. Payne, First principles methods using CASTEP, *Z. für Krist.-Cryst. Mater.* 220 (2005) 567–570, <https://doi.org/10.1524/zkri.220.5.567.65075>.
- [37] J.P. Perdew, K. Burke, M. Ernzerhof, Generalized gradient approximation made simple, *Phys. Rev. Lett.* 77 (1996) 3865–3868, <https://doi.org/10.1103/PhysRevLett.77.3865>.
- [38] S. Wang, L. Chen, X. Zhao, J. Zhang, Z. Ao, W. Liu, H. Wu, L. Shi, Y. Yin, X. Xu, Efficient photocatalytic overall water splitting on metal-free 1D SWCNT/2D ultrathin C₃N₄ heterojunctions via novel non-resonant plasmonic effect, *Appl. Catal. B: Environ.* 278 (2020), 119312, <https://doi.org/10.1016/j.apcatb.2020.119312>.
- [39] L. Chen, X. Zhao, X. Duan, J. Zhang, Z. Ao, P. Li, S. Wang, Y. Wang, S. Cheng, H. Zhao, F. He, P. Dong, C. Zhao, S. Wang, H. Sun, Graphitic carbon nitride microtubes for efficient photocatalytic overall water splitting: The morphology derived electrical field enhancement, *ACS Sustain. Chem. Eng.* 8 (2020) 14386–14396, <https://doi.org/10.1021/acssuschemeng.0c04097>.
- [40] G.L. Li, B.B. Yang, X.C. Xu, S. Cao, Y. Shi, Y. Yan, X. Song, C. Hao, FeNi alloy nanoparticles encapsulated in carbon shells supported on N-doped graphene-like carbon as efficient and stable bifunctional oxygen electrocatalysts, *Eur. J. Chem.* 26 (2020) 2890–2896, <https://doi.org/10.1002/chem.201904685>.
- [41] J. Wu, X. Yan, W. Wang, M. Jin, Y. Xie, C. Wang, Highly dispersed CoNi alloy embedded in N-doped graphitic carbon for catalytic transfer hydrogenation of biomass-derived furfural, *Chem. Asian J.* 16 (2021) 3194–3201, <https://doi.org/10.1002/asia.202100727>.
- [42] M.L. Brongersma, N.J. Halas, P. Nordlander, Plasmon-induced hot carrier science and technology, *Nat. Nanotechnol.* 10 (2015) 25–34, <https://doi.org/10.1038/nnano.2014.311>.
- [43] A.O. Govorov, H.H. Richardson, Generating heat with metal nanoparticles, *Nano Today* 2 (2007) 30–38, [https://doi.org/10.1016/S1748-0132\(07\)70017-8](https://doi.org/10.1016/S1748-0132(07)70017-8).
- [44] M. Cai, Z. Wu, Z. Li, L. Wang, W. Sun, A.A. Tountas, C. Li, S. Wang, K. Feng, A.-B. Xu, S. Tang, A. Tavasoli, M. Peng, W. Liu, A.S. Helmy, L. He, G.A. Ozin, X. Zhang, Greenhouse-inspired supra-photothermal CO₂ catalysis, *Nat. Energy* 6 (2021) 807–814, <https://doi.org/10.1038/s41560-021-00867-w>.